Mapping small and medium-sized water reservoirs using Sentinel-1A: a case study in Chiapas, Mexico

Alejandra A. López-Caloca,[a,b,]* Boris Escalante-Ramírez,[b] and Pilar Henao[a]

[a]Centro de Investigación en Ciencias de Información Geoespacial, Ciudad de México, México City, México
[b]Universidad Nacional Autónoma de México, Ciudad Universitaria, Facultad de Ingeniería, México City, México

Abstract. Using satellite data to study small water bodies (SWB) and medium-sized water bodies (MSWB) is extremely useful for understanding their status, how to conserve them as water reservoirs, and their vulnerability to climate variability. The images studied in our work correspond to different-sized lagoons located in areas with high and low topography in a tropical region of Chiapas, Mexico. Our research project delineates SWB and MSWB. For this analysis, we considered water bodies to be uniform regions in a synthetic aperture radar image. The robustness of the method was determined based on an analysis of the morphologies of 23 lagoons. Several methods, including Hermite transform, were analyzed and compared with other image denoising methods used to improve speckle reduction. To obtain additional spatial information for image classification, we analyzed texture using the gray-level co-occurrence matrix. The results indicate that the Hermite filter is the best method for identifying water bodies. The advantage of this filter is the identification of local patterns such as edges and lines. It also preserves and improves aspects related to the homogeneity of water bodies, using the Hermite coefficient selection criteria for local pattern feature selection/extraction. The lake water extent products demonstrate that Sentinel-1 is useful for identifying SWB in this study area. The results show very high detection of water bodies, with adequate detection for water bodies larger than 2 ha, and an area accuracy of 80%. © 2020 Society of Photo-Optical Instrumentation Engineers (SPIE) [DOI: 10.1117/1.JRS.14.036503]

1 Introduction

Water bodies are systems that store fresh water. Their natural ecological state depends on variables such as air, rainfall, evapotranspiration, aquifer recharge, and surface and groundwater runoff. With regard to their ecology, medium-sized water bodies (MSWB) and small water bodies (SWB) have a great diversity of flora and fauna,[1] particularly when they are located in natural settings where human intervention has been scarce. Because of the size of these water bodies and their seasonal changes in water storage capacity, they are considered to be indicators of the state of a territory and help in understanding climate variability. Depending on their geographic location, under local natural conditions, these water bodies can change in size or can form a system of multiple water bodies.

Unfortunately, due to human activities such as tourism and agriculture, the ecological condition of these reservoirs is becoming vulnerable. Kelly-Quinn et al.[2] stated that there are multiple views of conservation and different uses of these natural resources, which indicates a need to identify research priorities to better protect SWB. They suggest a need to continue researching conditions related to water surface extension. While global remote sensing methodologies are

*Address all correspondence to Alejandra A. López-Caloca, E-mail: alopez@centrogeo.edu.mx

valid for geographically large territories, for detailed scales such as the case of SWB, their ability to identify medium and small lakes on the land surface is limited. In the case of satellite images obtained with data from optical sensors, it is difficult to find products that are not affected by clouds. For this reason, maps of continental water bodies are generated for a particular observation period, for example, annual. The purpose of these thematic products is to quantify continental water resources at global and regional scales to provide a synoptic view.[3] Meanwhile, several studies have demonstrated the usefulness of synthetic aperture radar (SAR) data for identifying the surface of water bodies, such as rivers, lakes, coastal waters,[4] and for monitoring floods.[5,6] Because SAR can observe and capture information in day or nighttime conditions and can record the land surface regardless of cloud cover, its data are extremely useful for monitoring water bodies and for continuously updating existing cartography. SAR images can detect water bodies because of the physical principle behind how the radar sensor detects water surfaces, namely, the high contrast in the backscattering of the sensor's response. There are other factors that modify the return signal to the sensor, such as changes in lake surfaces when calm water becomes wavy due to wind or rain. In these cases, the return signal to the sensor detects backscattering as a nonhomogenous zone.[7]

The new satellite series provides good spatial and temporal resolution, which is useful for some of the ranges in the mapping of small and medium-sized lakes. The launching of the European Space Agency's (ESA) Sentinel-1 (S1) and Sentinel-2 (S2) missions is enabling new processing initiatives to be applied to the study of MSWB and SWB (streams, small lakes, and ponds). Various investigations state that water bodies are considered to be SWB when their maximum size is between 1 and 10 ha.[8] Pôssa and Maillard[9] showed that S1 data result in good delimitation of SWB in an urban area. They also obtained good results using a support vector machine (SVM) for the classification. Their study included three individual water bodies, one that measured 183 ha and two others with an approximate size of <7 ha.

This study provides an analysis of the lake water extent (LWE) for SWB and MSWB to improve their delimitation and detection. This LWE study analyzes the Montebello Lagoon system in Chiapas, Mexico, which is a small region covering several square kilometers. This system includes several different-sized water bodies. Their water surfaces are divided into two groups: 300 to 8 ha and 3 to 2 ha.

We propose a new strategy to delineate water bodies with good precision. This proposal takes into account the configuration of the S1 sensor and makes it possible to separate the water class as a homogenous region, where all pixels within the water body are assigned to water and the border pixels separate the water/nonwater region with well-defined edges. This methodology includes a preprocessing stage that is designed to use different noise reduction algorithms. During this stage, data preparation affects the classification of results. In an effort to reduce noise, different despeckling algorithms[10] were used, including the Lee filter, gamma maximum a posteriori (MAP) filter, Frost filter, and Hermite filter.[11] This last one was shown to be an effective tool for detecting and extracting characteristics such as edges and lines. Along with the noise reduction algorithm analysis, this study also assessed the potential use of texture parameters to estimate water body surfaces. The texture feature provides information on the spatial distribution of backscattering coefficient variations in a water body and between neighboring nonwater pixels. Several authors suggest using different SAR textures obtained with the gray-level co-occurrence matrix (GLCM) to monitor continental water bodies and to increase the feasibility of obtaining water/nonwater masks.[12,13] However, even though GLCM can identify the pattern of a water body, we still need to determine whether the texture feature improves the identification of patterns in SWB and MSWB. Thus, we propose a set of tests to find the best method to determine LWE, in combination with the classification of the SVM algorithm. These tests can be applied after selecting the best noise reduction algorithm and evaluating and assigning the different Haralick texture features. To evaluate the results, we propose calculating the indicators of area accuracy (AA) for each water body surface and comparing those with a reference map generated with S2 data.

This work is structured as follows. Section 2 presents the study site and describes the characteristics of the images that were used. Section 3 describes the bases for the noise reduction methodologies, the calculation of GLCM, the extraction and preparation of the data, and the analysis metrics used to evaluate precision. In Sec. 4, the findings obtained with the LWE maps

are shown for each lake and the results of the accuracy assessment are presented. Lastly, Sec. 5 discusses the most relevant conclusions.

2 Study Area and Dataset

2.1 *Study Site*

The study area is located in a region with a group of different-sized lagoons, composed of more than 50 water bodies (Fig. 1).[14,15] This system covers territory in Mexico and the Republic of Guatemala. The lagoons have a great biological diversity and are used in different ways by the nearby inhabitants, depending on the local context and sociocultural activities, such as agriculture, tourism, and recreation. They are located in the south-southeastern region of the state of Chiapas, where one of the studied lagoons—Laguna Internacional—crosses the border with Guatemala.

The water bodies of the Montebello Lagoon are of the lentic type (standing water and non-flowing), having no movement. These lakes are part of a karstic system in high and medium mountains. The Montebello Lagoon system has forms that are called uvala and doline, as may be
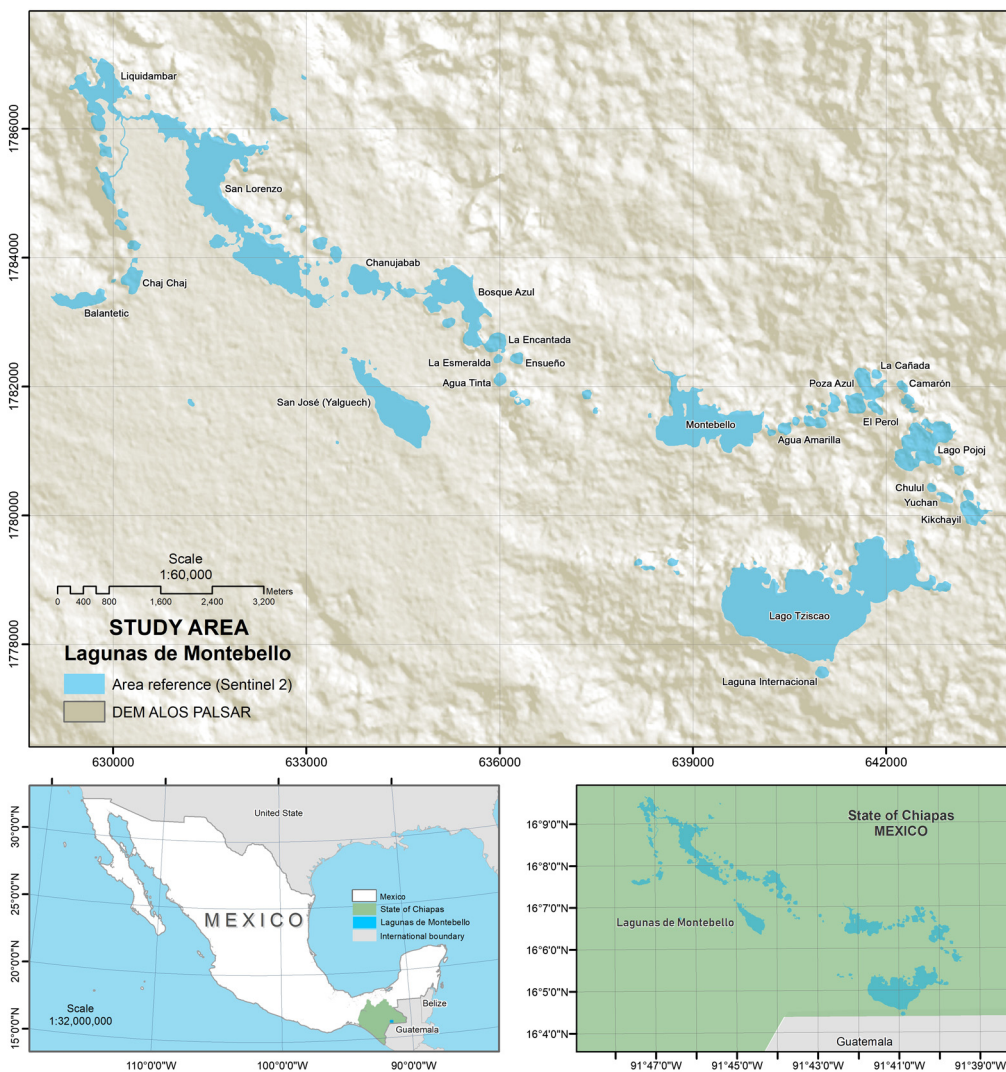
Fig. 1 Location of the study area corresponding to the Montebello Lagoons. A lagoon system is seen with water bodies of different sizes and shapes. Background: ALOS PALSAR (12.5 m) digital model for the terrain.

Fig. 2 Images of the natural conditions of some high mountain lagoons in the study zone.

seen in the map of geomorphological characteristics of the Montebello Lagoons National Park.[16] Dolines are water bodies that have rounded to elliptical surfaces, and uvalas are surfaces with shapes that are mainly elliptical.

Some lakes are connected by climatic conditions and seasons such as the rainy season (see Fig. 2). The lakes with the greatest extension are San Lorenzo, Montebello, and Lago Tziscao. The subsystem known as five lakes is formed by La Cañada, Agua Escondida, Peña Blanca, El Caracol, and El Perol. During heavy rainy seasons, their surfaces are connected.

2.2 Radar Data

S1 data were used to obtain water/nonwater binary masks. The characteristics of the products that were used are as follows: sensor SAR type = C-band SAR (5-cm wavelength); product type = ground range detection (GRD); polarization = dual (VV: transmitted vertically, received vertically and VH: transmitted vertically, received horizontally); equivalent number of looks (ENL) = 4.4; number of looks in range × azimuth = 5 × 1; spatial resolution $(m) = 20.4 \times$ 22.5 m in the ground range and azimuth direction; and pixel spacing (m) in range × azimuth = 10×10 in ground geometry. The S1 images are identified as S1A_IW_GRDH_1SDV_ 20190212T120153_20190212T120218_025896_02E210_2986_HT.data (S1A), in descending orbit with the acquisition date of February 12, 2019, and time of 12:01:53; and S1B_IW_ GRDH_1SDV_20190209T001348_20190209T001413_014862_01BBD1_535D_HT.data (S1B), in ascending orbit with the acquisition date of February 9, 2019, and time of 00:13:48.

2.3 Digital Terrain Model

The digital terrain model used for terrain correction was the ALOS Phased Array Type L-band SAR (PALSAR) with a 12.5-m resolution, downloaded from the Alaska Satellite Facility Distributed Active Archive Center.[17] This model is used for the process of correcting geometric and radiometric distortions in the radar signal. The information on the terrain in the study area corrects the slope, which decreases the shadow effect (ID: ALPSRP254270310-RTC_HI_RES).

2.4 Sentinel-2 Data

The water/nonwater binary masks obtained with SAR were compared with a synthetic reference water/nonwater binary mask obtained with S2 data. This optical image has a spatial resolution of 10 m. To prepare the reference image, three cloudless S2 images were acquired and evaluated during the month of the study. They were atmospherically corrected using the Sen2Cor module (S2 atmospheric correction) from the Sentinel Application Platform (SNAP) toolbox. Also using SNAP, all image bands with a 10-m spatial resolution were resampled. The dates of the images analyzed are S2B_MSIL2A_20190212T163409, S2A_MSIL2A_20190217T163341, and S2B_ MSIL2A_20190314T163039. The S1 and S2 images were obtained from the Copernicus

Table 1 Reference data for each lake in the Montebello Lagoon system (February 12, 2019).

Lagoon/lake	Altitude max. (masl)	Area (ha)	Lagoon/lake	Altitude max. (masl)	Area (ha)
	Group 1			Group 2	
Lago Tziscao	1515	307.635881	El Perol	1561	3.321428
San Lorenzo	1487	183.6146	Agua Amarilla	1519	3.296636
Montebello	1516	99.001221	Internacional	1499.5	3.071955
San José (Yalguech)	1453	62.7603	Agua Tinta	1484	3.059546
Bosque Azul	1452	55.066606	Ensueño	1494	2.905777
Lago Pojol	1536	43.431093	Yuchan	1521	2.706607
Liquidambar	1470	42.6059	Camarón	1534	2.150318
Poza Azul	1535	21.160164	La Cañada	1549	1.908817
Chanujabab	1453	20.950135	Chulul	1519.5	1.597041
Balantetic	1476.5	14.949466	La Esmeralda	1473	1.521229
Kikchayil	1513	12.84627	—	—	—
Chaj Chaj	1458.5	9.765615	—	—	—
La Encantada	1489.5	8.145258	—	—	—

website.[18] To verify the superimposition of the images obtained with S1 and S2 by date, color RGB compositions were generated to confirm that there was no geographic displacement. The segmentation was previously carried out with the sentinel water mask (SWM). This index, proposed in Ref. 19, selects the two bands with the highest reflectance for water—blue (B2) and green (B3)—and the two with the lowest reflectance—NIR (B8) and SWIR (B11). The index formula is SWM = blue + green/NIR + SWIR. Lastly, the binary mask maps obtained based on the SVM classification were consistent, and no changes in LWE among the three dates were identified. To determine the reference water mask, the date selected was the one closest to the date of the S1 ascending image and the S1 descending image. The resulting acquisition date of February 12, 2019 was selected. The vector information was then generated. Figure 1 shows the reference data. Table 1 shows the reference data for the 23 study lakes in the Montebello Lagoon system, measured in ha. All calculations were measured in m^2. These lakes are located at a maximum altitude of 1470 to 1560 masl.

3 Methods

The main methodological steps include: preprocessing, the water feature extraction test, and accuracy assessment. Figure 3 shows a diagram of the general procedure used for LWE. Water bodies were detected with GRD product images. The Sentinel-11A and 11B images were processed with free SNAP software. The SNAP, developed by ESA, was used for preprocessing, calibration, filtering, GLCM, and visualization.

3.1 Preprocessing of Radar Data

3.1.1 Application of orbit file and thermal noise removal

As shown in the preprocessing block in Fig. 3, orbit updating was applied first. This is done because the metadata file is first generated as a provisional file that includes the acquisition
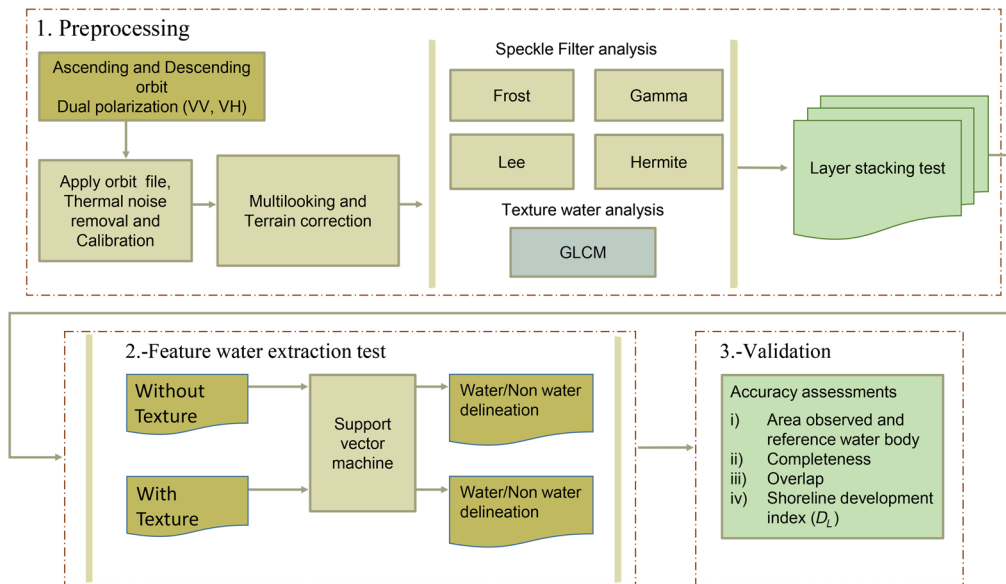
Fig. 3 Summary of experiments carried out in this study. First, the preprocessing block; second, the feature water extraction; and finally, the validation block.

parameters in a general way. The precise satellite orbit file is generated a few days later, and it then becomes necessary to update the file to what is called precise orbit ephemerides, which is found on the S1 Payload Data Ground Segment webpage.

Through thermal noise removal, thermal noise is eliminated to remove values that are seriously affected by this type of noise, which can be present at the edges of an image or in discontinuities in the inter-subswath.

3.1.2 Calibration

The SAR images $Y(x, y)$ were calibrated by transforming the values from digital numbers to backscattering coefficient units—sigma nought value (σ^0). This value represents the power returned to the antenna from the ground for each polarization (VV and VH).

3.1.3 Speckle filtering of SAR images

With SAR image capture, speckle noise makes it more difficult to visually interpret images and reduces the effectiveness of the segmentation and classification algorithms. There are two ways to reduce speckle: multilook processing and spatial filtering. In this work, we applied several spatial filtering techniques. Methods that use spatial filtering to reduce speckle noise are aimed at achieving a balance between speckle reduction and the amount of detail that is needed to preserve a particular application. Speckle noise affects images of homogenous zones, leading to the appearance of textural differences. Rayleigh defined a criterion to determine when to consider a surface to be rough and when to consider it flat. A surface is considered to be rough when $H \geq \lambda/(8 \cos \theta)$, where H is the height at which the sensor is located, λ is the observation wavelength, and θ is the angle of incidence. The amplitude, A, of the signal received by the radar is modeled as $A = \sqrt{I} = \sqrt{C_r^2 + C_i^2}$, where I is the intensity and C_r and C_i are the real and imaginary components of the signal received by the antenna, respectively. The amplitude of the SAR images is represented by a Rayleigh distribution that is given by the following equation:

$$p(A) = \frac{2A}{\sigma^2} \exp\left(-\frac{A^2}{\sigma^2}\right), \tag{1}$$

where $A \geq 0$, the mean is $\mu_1 = \sigma\sqrt{\pi}/2$, and the variance is $\sigma_1^2 = (4 - \pi)\sigma^2/4$. Based on these expressions, it is possible to obtain the signal-to-noise ratio (SNR) for one-look amplitude.

$$\text{SNR} = \frac{\mu_1}{\sigma_1} = \sqrt{\frac{\pi}{4-\pi}} \approx 1.9131. \tag{2}$$

Speckle noise in SAR images is generally described as a multiplicative model. The SNR for multilook is $\text{SNR}_{Nlooks} = 1.9131\sqrt{N_{\text{look}}}$.

The ideal filter does not lose any information when reducing speckle. For example, in homogenous areas, the filter must preserve the radiometric information and the edges between the different areas in textured zones. When reducing speckle, adaptive speckle filters take into account changes in the local properties of terrain backscattering. To adapt, these filters use the local intensity of the scene (the mean intensity of the pixels of the moving window filtering) and its local variation. That is, an adaptive speckle filter adapts to local variations in the intensity of the image. In general, filters that use small windows (3×3 or 5×5) better preserve texture information.

Lee filter. With the Lee filter, a linear model is used to analyze the multiplicative model. The Lee filter is based on the minimum mean-square error (MSE) criterion. The calibrated and despeckled image (Y^0) is formulated as

$$Y^0(t) = Y_c(t)W(t) + Y_m(t)[1 - W(t)], \tag{3}$$

where $Y_c(t)$ is the backscattering intensity value of the central pixel in the filter kernel, $Y_m(t)$ is the backscattering intensity value of the pixels not in the filter window, $W(t) = \frac{(1-C_u^2)}{C_Y^2}$ is the weighting function, $C_u = \sqrt{\frac{1}{N_{\text{look}}}}$ is the coefficient of variation (C_u) of the estimated noise with N_{look} being the number of looks, $C_Y = \frac{\sigma}{Y_m(t)}$ is the C_v for the image, and σ is the standard deviation of the backscattering intensities without the window.

To spatially filter each individual pixel in an image, the backscattering coefficient values (σ^0) are used within a 3×3 filter window. The pixel value is the weighted sum of the observed (central) pixel value and the average value. The weighted coefficient is a function of the local heterogeneity of the terrain, measured in terms of the C_v. In practice, this filter requires the local C_v to be estimated for each scene.

Frost filter. This algorithm is based on convolving the SAR image with the adaptive impulse response function. The Frost filter replaces the local pixel of interest with a weighted sum of the values with an *n-x-n* moving window. The weight factor decreases with the distance of the pixel of interest. This filter assumes multiplicative noise and stationary noise. The formula is given by

$$m(t) = e^{-KC_u^2(t_o)|r|}, \tag{4}$$

where K is the constant that controls the attenuation factor of the impulse response function, t_0 refers to the pixel to be filtered, and C_u is the coefficient of variation.

This filter uses an exponentially attenuated convolution kernel that adapts to the local C_v. The impulse response of the SAR system is obtained by minimizing the MSE between the observed image and the reflectivity of the scene. As in the previous case, the N_{look} parameter is used to estimate the noise variance and to control the amount of smoothing that the filter applies to the image.

Gamma filter. This filter is based on the supposition that the scene intensity has a gamma distribution. Similar to the Frost and Lee filters, this filter minimizes the loss of textural information and is appropriate for scenes with features that represent a Gaussian distribution, such as tree-covered areas, agricultural zones, and oceans.

Kuan[20] first proposed the use of the gamma MAP filter to reduce speckle noise. The application of this filter requires *a priori* knowledge of the scene's density probability function. Kuan assumed a Gaussian distribution for this probability density function. Lopes[21] modified the Kuan MAP filter by assuming that the scene has a gamma distribution, and two thresholds were established. The gamma MAP filter result is given as

$\overline{S}(t_0) = [(\alpha - N_{\text{look}} - 1)\overline{Y}(t_0) + \sqrt{\overline{Y}^2(t_0)(\alpha - Y - 1)^2 + 4\alpha N_{\text{look}}\overline{Y}(t_o)}]/2\alpha$, for $C_u \leq C_Y(t_0) \leq C_{\text{max}}$, where N_{look} is the number of looks, $C_{\text{max}}(t_0) = \sqrt{2C_u}$, $\alpha = 1 + C_u^2/C_Y^2(t_0) - C_u^2$, and $C_u = \sqrt{1/N_{\text{look}}}$. For $C_Y(t_0) < C_u$, and $C_Y > C_{\text{max}}$, $\overline{S}(t_0) = \overline{Y}(t_0)$ and $\overline{S}(t_0) = Y(t_0)$, respectively.

Hermite transform.   This study used the Hermite transform (HT) as an algorithm for noise reduction.[11,22] This algorithm adapts to the statistical characteristics of images. HT is a decomposition technique for n-dimensional signals (such as an image) that projects a window localized image on an orthogonal basis composed of the Hermite polynomials. This method can be described by the following steps.

i. Forward polynomial transform.

The input SAR image, defined as $Y(x, y)$, with (x, y) coordinates, is multiplied by a $V(x - p, y - q)$ window function at all (p, q) positions. The polynomial transform is defined by the following function:

$$Y(x, y) = \frac{1}{W(x, y)} \sum_{p,q \in S} Y(x, y)V(x - p.y - q), \quad (5)$$

where $W(x, y)$ is a weighting function equal to $\sum_{(p,q) \in S} V(x - p, y - q)$ and S is the sampling lattice and is related to the complete signal description through the windowing mapping process. This process is carried out at several equidistant positions on the image. In addition, a necessary condition for the weighting function is to be different from zero for all (x, y). The next step is to approximate the localized signal within the window $V(x - p, y - q)$ with an orthogonal polynomial expansion. To calculate the polynomial coefficients $Y_{m,n-m}(p, q)$, the $Y(x, y)$ image is convoluted with the $D_{m,n-m}$ filter as follows:

$$Y_{m,n-m}(p, q) = \int_{-\infty}^{+\infty} \int_{-\infty}^{+\infty} Y(x, y)D_{m,n-m}(p - x, q - y)\mathrm{d}x\,\mathrm{d}y \quad (6)$$

for $m = 0, \ldots .n$ and $n = 0, \ldots .N$. The filter is expressed as $D_{m,n-m}(x, y) = G_{m,n-m}(-x, -y)V^2(-x, -y)$, where $G_{m,n-m}(x, y)$ is the polynomial of m degree in x and $n - m$ in y. N is the maximum order of the polynomial expansion.

ii. Inverse polynomial transform.[23]

The resynthesized image $Y'(x, y)$ is obtained by

$$Y'(x, y) = \sum_{n=0}^{N}\sum_{m=0}^{n} \sum_{(p,q) \in S} Y_{m,n-m}(p, q)P_{m,n-m}(x - p, y - q), \quad (7)$$

where $P_{m,n-m}(x, y) = \frac{G_{m,n-m}(x,y)V(x,y)}{W(x,y)}$ is the interpolation function for $m = 0, \ldots, n$ and $n = 0, \ldots N$ and the weighting function is given by $W(x, y) = \sum_{(p,q) \in S} V(x - p, y - q)$.

iii. HT.

The HT resembles some of the characteristics of human vision. It is based on the analysis of images with Gaussian derivatives and local processing. The HT is a special case of a polynomial transform in which the local analysis window $V(x, y)$ is the Gaussian function. In this case, the associated orthogonal polynomials are the Hermite polynomials.

$$G_{n-m,m}(x, y) = \frac{1}{\sqrt{2^n(n - m)!m!}} H_{n-m}\left(\frac{x}{\sigma}\right)H_m\left(\frac{y}{\sigma}\right), \quad (8)$$

where $H_n(x)$ is the n'th Hermite polynomial of degree n in x.

The decompositions consist of a number of subimages that represent a low-pass residual known as zero-order coefficients $(Y_{0,0})$ and several high-pass bands containing detailed information coefficients, where $Y_{0,1}$ and $Y_{1,0}$ are the first-order coefficients for SAR images.
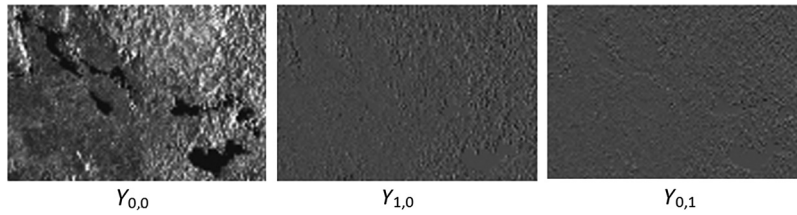
Fig. 4 Detailed images of zero-order coefficients ($Y_{0,0}$) and first-order coefficients ($Y_{1,0}, Y_{0,1}$).

$Y_{0,2}$, $Y_{1,1}$, and $Y_{2,0}$ are the second-order coefficients for SAR images, respectively, and so on, until the highest coefficient order, N. The zero-order coefficient $Y_{0,0}$ represents a smooth version of the original image. A rotated version of the HT was proposed in Ref. 24. This version locally adapts the coordinate axes of the HT to the orientation of edges.

Figure 4 shows an HT expansion of a SAR image. The original image is decomposed into a number of subimages that consist of a low-pass (approximation) image with a zero-order coefficient ($Y_{0,0}$) and a series of high-pass coefficients containing detailed information that correspond to first- and second-order HT coefficients.

iv. Adaptive noise reduction in SAR images.

As described in Refs. 11 and 22, the noise reduction method consists of adaptively blurring the image. First-order HT coefficient energy $Y_{1,0}^2 + Y_{0,1}^2$ is used to detect relevant edges in the image. To discriminate between edges and noise in the energy measure, an adaptive local threshold is set. Because speckle noise can be modeled as multiplicative, noise variance is proportional to the local mean value; therefore the local threshold is determined by

$$T = 2\alpha \frac{\mu_Y^2}{AN_{\text{look}}} \ln\left(\frac{1}{P_r}\right), \tag{9}$$

where α is a proportionality constant, μ_Y is the local mean of the original image, A is the SNR, N_{look} is the number of looks of the $Y(x, y)$ image, and P_r is the probability of noise in the image and is defined by the user (for example, 0.5).

This adaptive, moving threshold results in a binary mask that shows the locations of edges that are relevant to the user's parameters. This binary mask is multiplied by the higher-than-zero-order HT coefficients so that, after the inverse HT transform is performed, noisy regions in the image can be reconstructed with the zero-order HT coefficient only, while regions with edges can be fully reconstructed, thereby preserving sharpness. A more elaborated method involves a multiresolution approach that enables detecting edges at different spatial scales as well as using the rotated HT.[24,25] This makes it possible to reduce noise not only in homogeneous regions but also on the edges, resulting in sharper images.

The HT algorithm was implemented with MATLAB version 7.0. To restore the images, the experimental processing parameters used were as follows: noise type = multiplicative, noise to eliminate $(1 - P_r) = 15\%$, number of looks = 1, polynomial transform parameters = directional processing, window length = 4, subsampling period = 2, and pyramid levels = 1.

The filters were evaluated for their ability to reduce noise by computing the C_v and the equivalent number of looks (ENL), and preserving edges as measured by edge preservation degree-ratio of average (EPD-ROA). The EPD-ROA[26] was calculated by the following equation:

$$\text{EPD}_{\text{ROA}} = \frac{\sum_{i \in Y} |E_{D1}(i)/E_{D2}(i)|}{\sum_{i \in Y} |E_{O1}(i)/E_{O2}(i)|}, \tag{10}$$

where Y is the image information, $E_{D1}(i)$ and $E_{D2}(i)$ are the adjacent pixel values of the despeckled image in horizontal or vertical orientations, respectively, and $E_{O1}(i)$ and $E_{O2}(i)$ are the corresponding adjacent pixel values along a certain orientation of the original image and that of the speckled image for real data.

Logarithmic transform is used to convert the backscattering coefficient to decibels (dB),[27] and the denoising images are geometrically corrected before calculating Haralick texture descriptors.

3.1.4 *Water texture analysis*

There are various Haralick texture descriptors that indicate the behavior of water body surfaces. For example, a homogeneous region is considered "calm water," seen as white or dark color, and the segmentation contains a "solid area." When there is "rough water" within a water body, the spatial relationships between two internal pixels are different and are seen as a gradient of gray levels. When this happens in the image segmentation process, it leads to a "holes in the lake" effect.

The Haralick model was calculated based on the following parameters found in the SNAP tool developed by the ESA. First, a 5×5 window size was used, where the spatial relationship between neighbors was defined to avoid loss of details. With regard to spatial relationships, angles were selected in four directions: horizontal, vertical, diagonally up, and diagonally down. The quantization included 32 levels. Displacement or distance was 2, which refers to the distance between a pair of pixels (reference and neighbor). Generally, texture descriptors provide the same type of information and are correlated, some positively and others negatively.

Texture descriptors were selected based on visual interpretation, the content of the textural information, and correlation. Four texture measurements were calculated in this work: GLCM_mean, entropy, energy, and GLCM_contrast. GLCM_mean is a statistical texture descriptor that has a filtering effect that reduces speckle noise, but there is a loss in edge sharpness. It smooths the water surface, generates pixels that are very similar, and favors the identification of homogenous zones, which contributes to distinguishing water from nonwater pixels. GLCM_mean is highly correlated with the homogeneity feature. Entropy indicates variations in intensity. Negative entropy values indicate that there are more ordered elements, which are interpreted as homogenous zones. For this reason, the interface edge or outline of a water body is expected to be highly distinguishable and quantifiable. Energy indicates a uniform backscattering coefficient throughout the water body and is highly correlated with the homogeneity descriptor. Contrast is more commonly associated with the visual characteristics of edges, and it highlights changes in water and nonwater borders.

3.1.5 *Layer stacking test*

This analysis is based on a stack of textures with no texture images. Twelve general tests were conducted, some of which took into account aspects related to texture. Table 2 lists and describes the tests that were generated as input for the SVM algorithm.

3.2 *Water Extraction Feature*

Unlike other supervised classifiers, the SVM algorithm is based on the distribution of the data used to assign a pixel to a class. The SVM classifier uses a geometric criterion that takes into account the maximum margin between classes. An optimal hyperplane is defined as the maximum separation between classes, which depends on the multidimensional space available for processing. That is, for multispectral images, it depends on the number of bands to be classified by the SVM algorithm. With the training data, the SVM algorithm is transformed into a vector space with a greater dimension. This process is performed with a kernel by which the separation hyperplane is generated. Different types of margins and kernels (mathematical functions) exist, including separable linear, polynomial, and a radial basis function. The input parameters of the kernel are a constant (c) that penalizes the pixels that are located on the wrong plane and gamma (γ), which is proportional to the amplitude of the kernel. This study used SVM, which was implemented with the Montevedi (ORFEO-CNES) free software toolbox. The parameters include linear kernel function with a γ value of 1, border margin with a minimum of 1, and relationship between the training and validation data of 0.5.

In the case of SWB and MSWB, when using the classifying method to differentiate between water and nonwater borders, we need to consider that there are transition zones that may have a high degree of heterogeneity. The training phase and defining the number of classes are very

Table 2 Layer stacking tests.

Filter	Desc/asc orbit	Pol	GLCM-textural descriptor	ID
Lee	Yes	VV/VH	None	LEE-SIGMA0-DB-VV
				LEE-SIGMA0-DB-VH
Hermite	Yes	VV/VH	None	HERMITE-SIGMA0-DB-VV
				HERMITE-SIGMA0-DB-VH
Lee	Yes	VV/VH	Mean	LEE-GLCMMEAN-DB-VV
				LEE-GLCMMEAN-DB-VH
Hermite	Yes	VV/VH	Mean	HERMITE-GLCMMEAN-DB-VV
				HERMITE-GLCMMEAN-DB-VH
Lee	Yes	VH	Mean + entropy + energy	LEE-GLCMMEAN-ENTROPY-ENERGY-DB-VH
Hermite	Yes	VH	Mean + entropy + energy	HERMITE-GLCMMEAN-ENTROPY-ENERGY-DB-VH
Lee	Yes	VH	Mean + contrast	LEE-GLCMMEAN-ENTROPY-ENERGY-DB-VH
Hermite	Yes	VH	Mean + contrast	HERMITE-GLCMMEAN-CONTRAST-DB-VH

important for training the SVM classifier and for generating good class separation to obtain a water/nonwater binary mask. The nonwater class in this study includes bare soil, cities, agricultural land, grasslands, and forests. The water class includes the water pixels corresponding to each lake in the Montebello Lagoons system.

3.3 Assessing Accuracy

Water body indicators were analyzed based on the LWE maps to quantify the efficacy of the classification of each test studied. Using different methods, a vector cartography of the shapefile polygon was obtained by turning the binary mask into a vector. For each lake or reservoir, three assessment methods were used to evaluate precision: AA (%), completeness (%), and overlap. In addition, shape characteristics were measured using shoreline development (SLD) to understand the different morphologies of the 23 lagoons. The first method, AA, is based on the following equation:[9]

$$AA = \frac{a_{\text{ref}} - a_{\text{SAR}}}{a_{\text{ref}}} * 100, \tag{11}$$

where a_{ref} is the reference area and a_{SAR} is the area obtained from S1 data.

Quantitative precision was evaluated by calculating the indicators of completeness and overlap. Completeness[28] is defined as the ratio of the area extracted within the reference area to the reference area, given as a percentage.

$$\text{Completeness} = \frac{\text{area of extraction within reference}}{\text{area of reference}} * 100. \tag{12}$$

The overlap indicator[29] is defined as the total number of matching pixels from both regions (observed and reference) divided by the sum of the areas of the two regions. If both regions are identical in size, the overlap value is 1.

$$\text{Overlap} = \frac{2 * \text{intersection}}{\text{area1} + \text{area2}}. \tag{13}$$

Table 3 Results of the C_v, ENL, EPD-ROA-VD, EPD-ROA-HD, and AVE.

| | Descending orbit | | | | | | Ascending orbit | | | | |
Filter	Cv 3 × 3	ENL	EPD-ROA VD	EPD-ROA HD	AVE	Filter	Cv 3 × 3	ENL	EPD-ROA VD	EPD-ROA HD	AVE
Frost_VH	0.255	15.37	1.012	0.966	0.989	Frost_VH	0.254	15.50	0.994	0.989	**0.991**
Gamma-VH	0.245	16.66	1.002	1.002	**1.002**	Gamma-VH	0.244	16.79	0.988	0.985	0.986
Lee_VH	**0.124**	**65.04**	0.961	1.009	0.985	Lee_VH	**0.123**	**66.09**	0.960	0.964	0.962
HT_VH	**0.138**	**52.51**	1.018	0.982	**1.000**	HT_VH	**0.132**	**57.39**	1.004	0.992	**0.998**
Frost-VV	0.249	16.13	0.981	0.980	0.950	Frost-VV	0.243	16.93	0.984	0.983	0.983
Gamma-VV	0.242	17.07	1.003	1.005	**1.002**	Gamma-VV	0.236	17.95	0.998	0.996	**0.997**
Lee-VV	**0.129**	**60.09**	0.964	0.964	0.964	Lee-VV	**0.123**	**66.09**	0.967	0.967	0.967
HT-VV	**0.116**	**74.32**	1.006	0.974	**0.980**	HT-VV	**0.119**	**70.62**	1.030	1.004	1.032

Note: CV, coefficient of variation; ENL, equivalent number of look; EPD-ROA, edge-preservation degree based on the ratio of average; VD, vertical direction; HD, horizontal direction; and AVE, average EPD-ROA.

SLD measures the shape of a lake (in meters or feet). SLD is the ratio of the shoreline length to the circumference of a circle with an area equal to the area of the lake.

$$\text{SLD} = \frac{L}{2\sqrt{\pi A}}, \tag{14}$$

where L = shoreline length and A = surface area of the lake.

4 Results and Discussion

4.1 *Speckle Filter Analysis*

The special requirement of despeckle filters is that they preserve the edges of SWB. The problem with SAR images is speckle noise, which complicates the identification of edges. To detect a water surface, the edge of a lake needs to be well-defined and separable from the background (nonwater) pixels. Table 3 presents the performance of each algorithm based on the calculation of the C_V, ENL, and EPD-ROA. Figure 5 shows the details of the images that were filtered using the different methods.

As seen in Table 3, based on C_V, the best noise reduction results were obtained in descending mode with a Lee filter and for VH polarization, resulting in a C_V of 0.124. For the VV channel,
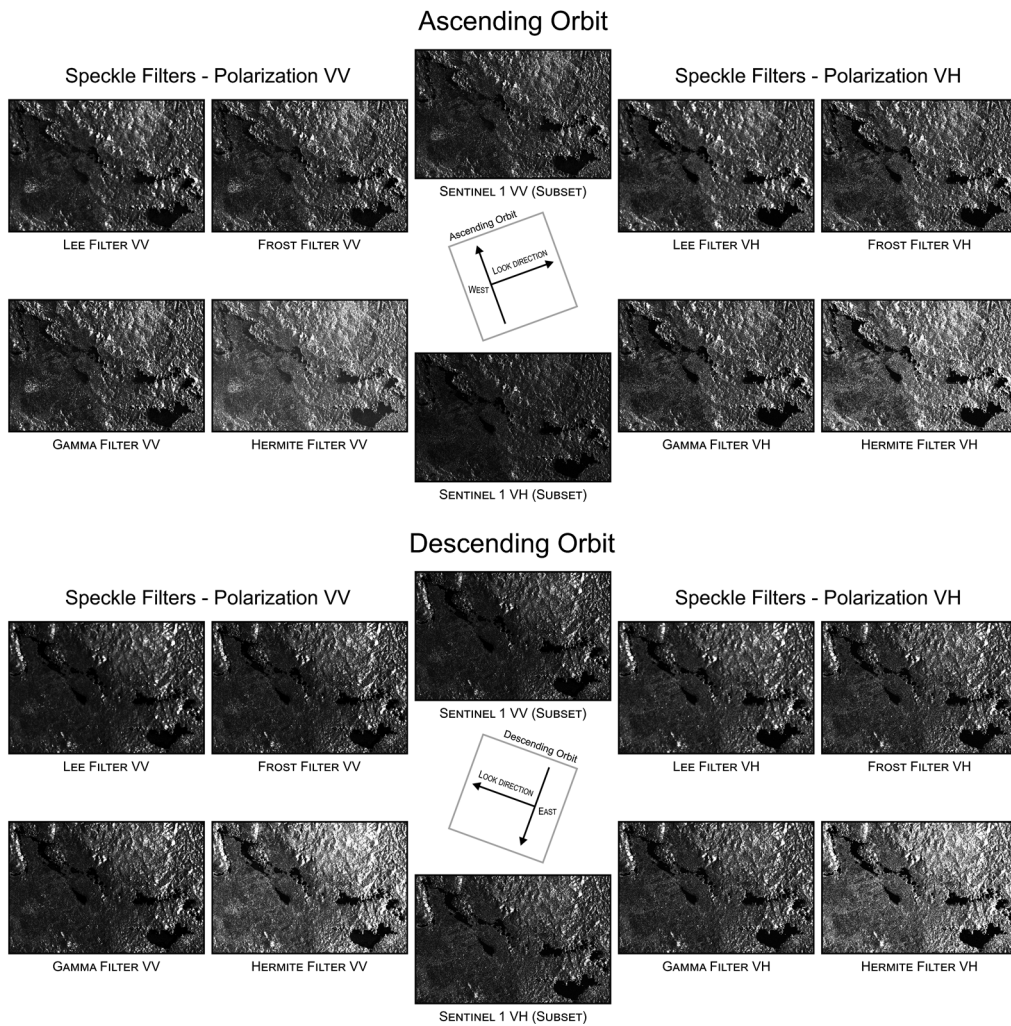
Fig. 5 Images resulting from noise correction with four filter methods. Descending and ascending orbits, VV and VH polarizations.

a C_V of 0.116 was obtained using the HT filter. With regard to ascending mode, the C_V was 0.123 with the Lee filter, for both VV and VH polarizations; with the HT filter, it was 0.119 for VV and 0.132 for VH polarizations. The ENL value is high when the quality of the denoising image is good. The calculation of ENL in this work resulted in high values for the HT filter. In all tests, the average EPD-ROA was between 0.96 and 1, which shows that the edges are well preserved. The best results were obtained with the gamma filter and the HT filter, shown in bold in Table 3.

We selected the two best noise reduction filters. A visual inspection identified the filters that best preserved the edges (Fig. 5). With the HT filter, we can see that the image is sharp, the edges are not degraded, and the homogenous zones with high backscattering intensities are smoothed. Image sharpness is achieved because of the directional adaptive nature of the HT method. First-order Hermite coefficients detect sharp edge positions and orientations, thereby smoothing only in the parallel directions of edges. This strategy not only reduces noise on the edges but also produces a sharpening effect.

As we can see from the previous findings, the quantitative values indicate that the Hermite and Lee filters result in the best speckle reduction according to C_v and ENL. The products that were obtained from these two filters were used to perform the subsequent tests.

4.2 *Analyses with Binary Water Mask*

Figure 6 shows the LWE maps resulting from each test, including both VV and VH polarizations, ascending and descending orbits, Lee and HT filters, and with and without texture. The 23 main lakes in each LWE map were analyzed to evaluate the classification of the 14 LWE maps that were obtained by the different methods presented in Table 2.

The surface properties and area (km^2) of each lagoon were determined for each LWE map. The areas obtained with S2 data served as reference areas for the accuracy assessment, as explained in Sec. 2.2. The radar chart in Fig. 7 shows the AA for each water body, so the areas can be easily compared. Each method is represented by a different color, and each axis corresponds to a lagoon.

We divided the 23 lagoons into two groups according to the surface areas of the lakes. The first group includes medium-sized lakes in which the water surface covers between 307.83 and 8.14 ha. This includes 13 lagoons that extend from Lago Tziscao to La Encantada. The second group includes the lagoons with surface areas between 3.32 and 1.52 ha, which were labeled SWB. This includes the remaining 10 lakes from El Perol to La Esmeralda (see Table 1). The radar charts in Figs. 7 and 8 show the lakes from biggest to smallest.

4.2.1 *Group 1: MSWB*

As seen in Fig. 7, for ascending orbit and VV polarization, the analysis of the areas in the radar charts shows a drastic decrease in the areas of the San Lorenzo, San José, and Chanujabab lakes. This could possibly be explained by the presence of a certain degree of roughness on the water surface resulting from natural winds that were present at the time of data acquisition. In ascending orbit, the data were acquired during the first seconds of the day. This result agrees with the visual evaluation of the LWE maps in Fig. 6. Visually, our findings show that, for the VV polarization and in ascending orbit, artifacts that look like holes in the lakes can be seen in these three lakes (San Lorenzo, San José, and Chanujabab). That is, the edges of these water bodies are not completely delimited, as seen in the LWE maps with the IDs LEE-SIGMA0-DB-VV, LEE-GLCMMEAN-DB-VV, HERMITE-SIGMA0-DB-VV, and HERMITE-GLCMMEAN-DB-VV. This agrees with what was reported in Ref. 30, namely, that the VV band is more sensitive to rough surface conditions. As seen in Fig. 6, with this water body size, VH cross polarization is less sensitive to surface effects that have a certain degree of roughness.

As shown in the radar charts in Fig. 7, in descending mode for both VV and VH polarizations, the AA ranges between 80% and 98% for the lakes extending from Tziscao to La Encantada. This may suggest calm water because the SAR data were acquired at mid-day.

With regard to the analysis of MSWB, the AA of the tests that used texture data (such as GLCM_mean and GLCM_mean with energy and entropy) were generally not better than the AA that resulted from the tests without texture. Nevertheless, they did generate homogenous internal
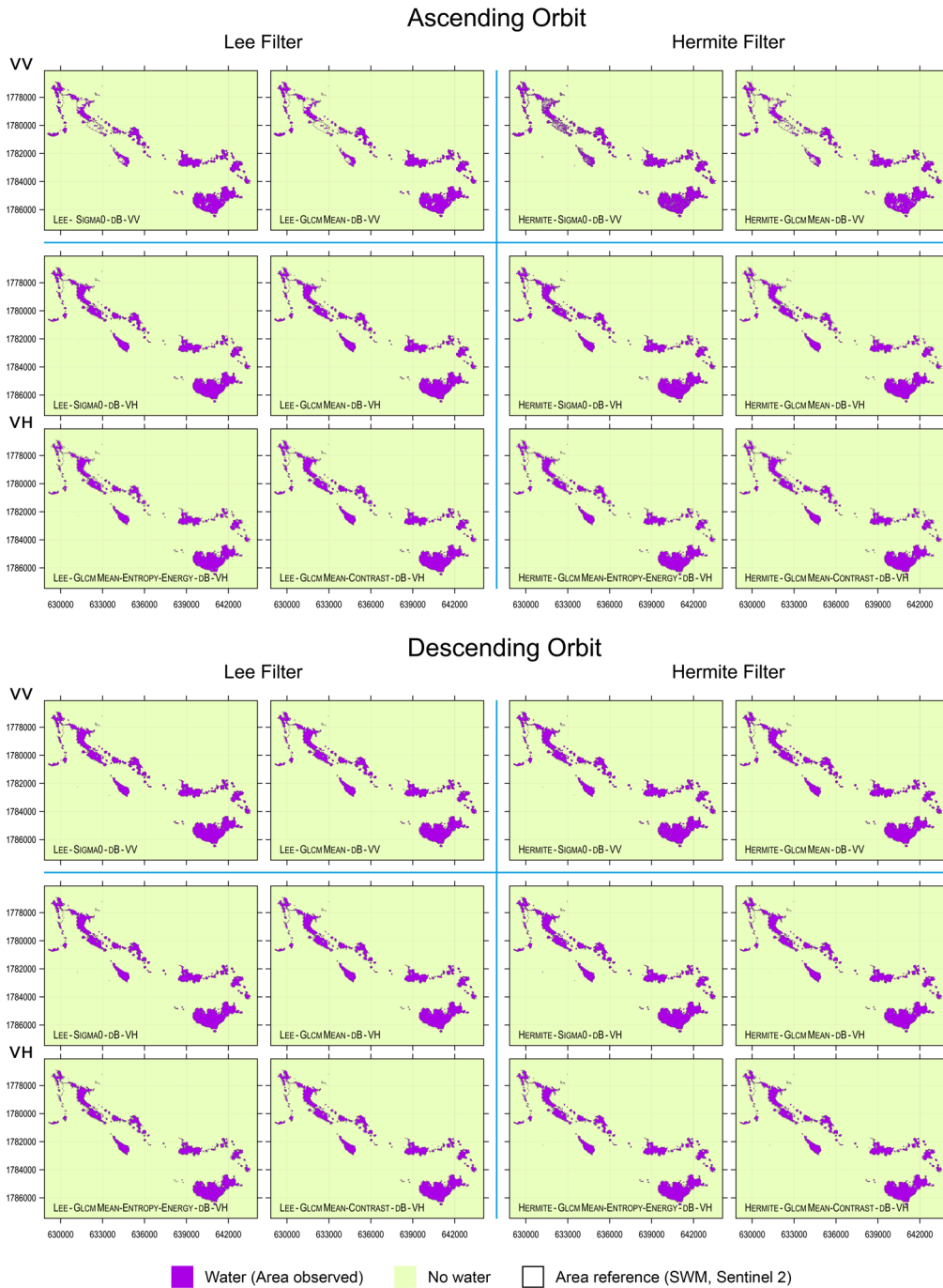
Fig. 6 Results of the LWE maps obtained with the different methods studied. The water masks obtained with each test are in purple. The reference water masks are delineated in a vector form (black).

areas in the water bodies, which were difficult to detect because of the rough water surface. Meanwhile, the percentages resulting from the tests with GLCM_contrast were lower than the tests with texture.

4.2.2 *Group 2: SWB*

Figures 6 and 7 show the results for SWB. Figure 7 shows the AA in the form of four radar charts for ascending and descending orbits. As can be seen, the descending orbit data underestimate VH
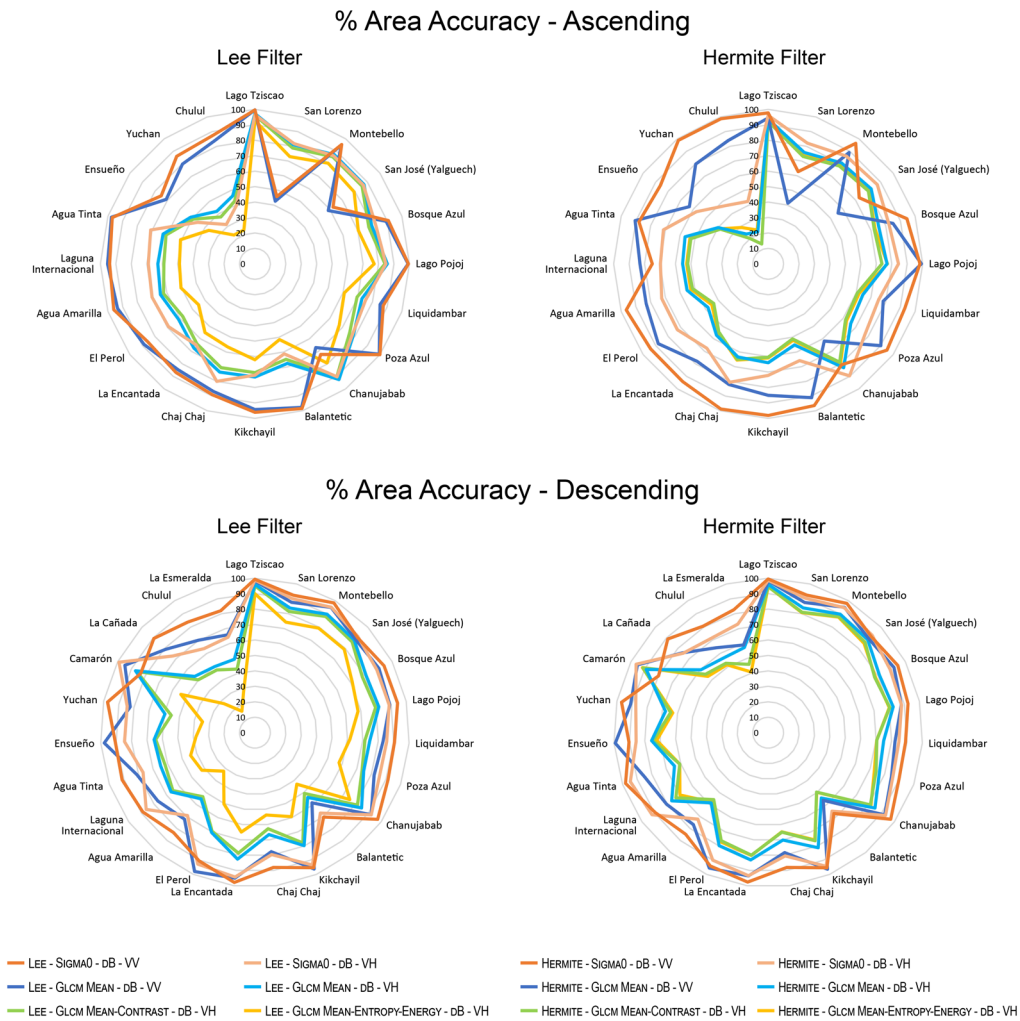
Fig. 7 Radar charts (radial net) of AA obtained with the tests studied for each lagoon, with and without texture, ascending and descending with Lee filter and Hermite filters. The La Cañada, Camarón, and La Esmeralda Lagoons were under 20% in ascending orbit and were not included in the chart.

polarization, which may be due to tree cover around these SWB. With VH polarization, there is greater variability in backscattering in tree-covered areas around a water body. For SWB, VV polarization better detects water body surfaces when there are no effects from roughness on the surface due to winds or heavy rain. In general, the results obtained with the GLCM matrix show that texture variables are very sensitive to the identification of the water body sizes that were analyzed in this study. This is in spite of the fact that the texture metrics that were used improved the uniformity of the water body pattern. The analysis of the texture descriptors suggests that texture parameters cannot be recommended for the delineation of SWB. As seen by comparing the radar charts shown at the bottom of Fig. 7, which present the AA in descending mode with Lee and Hermite filters, the six tests resulted in greater detail in AA with the Hermite filter than with the Lee filter.

Based on the above-mentioned results, a new set of LWE maps with high AA percentages was selected. This new set included the four LWE maps with the IDs LEE-SIGMA0-DB-VV, LEE-SIGMA0-DB-VH, HERMITE-SIGMA0-DB-VV, and HERMITE-SIGMA0-DB-VH.

The radar charts in Fig. 8 shows the calculations of the AA for ascending and descending orbits, completeness percentages, and overlap (descending orbit) for each lagoon. The SLD index was also determined for descending orbit. Table 5 (see the Appendix for details) presents data that compare the different measurements of precision and the SLD.
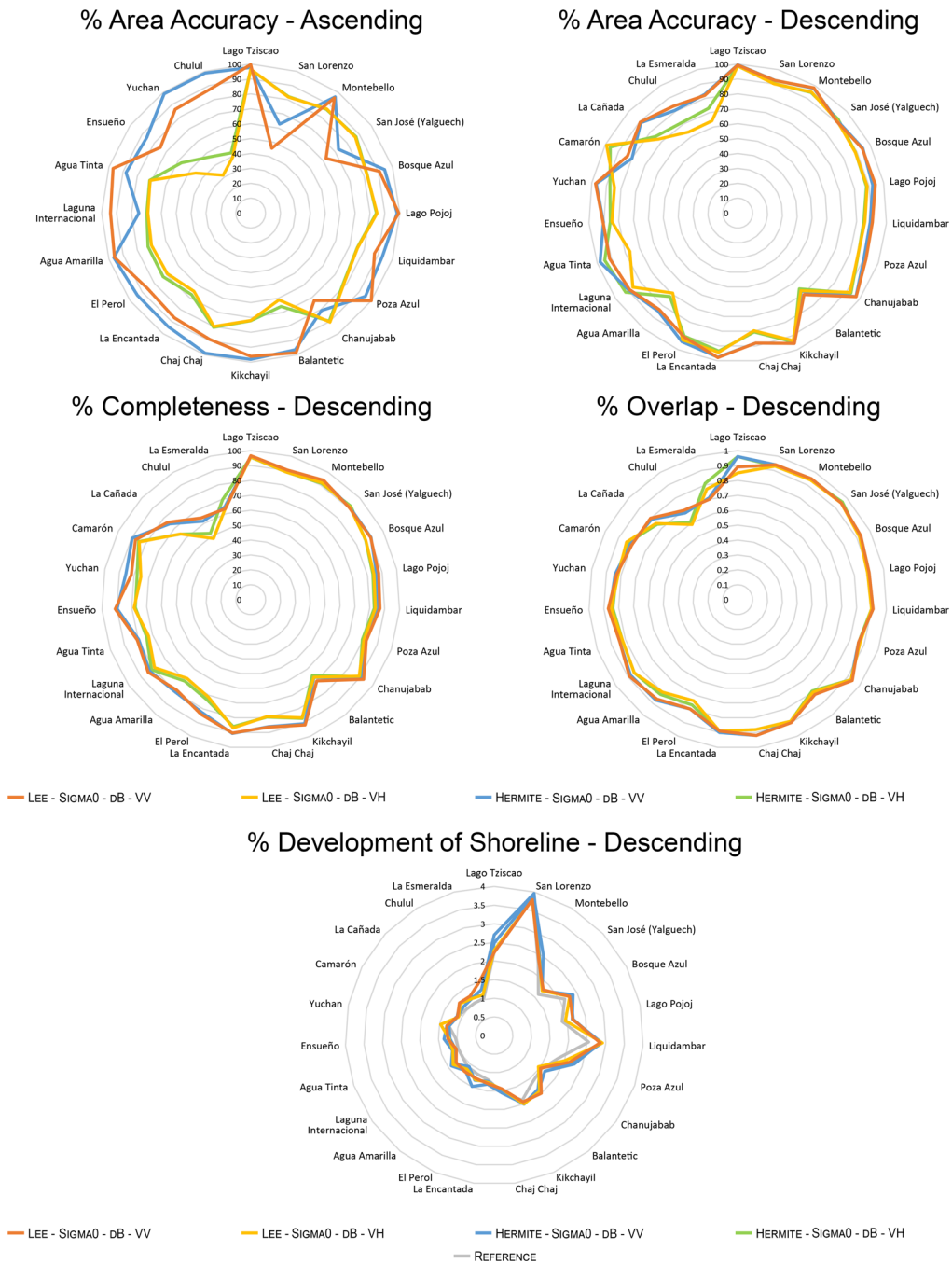
Fig. 8 A radar chart (radial net) of AA (%) (ascending and descending orbits), completeness (%), overlap, and shoreline development for descending orbit.

Figure 8 shows the AA in ascending and descending orbits. As can be seen, VV polarization had better results than VH polarization for most of the lakes studied. However, in ascending orbit, the La Cañada, Camarón, and Esmeralda Lagoons presented pixels with this pattern that were under 40% in area (not included in the chart).

With regard to descending orbit, the HT filter resulted in good AA (>80%) for VV and VH polarizations. As seen in Table 4 (see the Appendix for details), for VV polarization, 22 lakes had an accuracy of over 80% with the Hermite filter and 21 with the Lee filter (see Fig. 8).

For both polarizations, the completeness percentage is between 80% and 100% for most of the lakes. Also for both polarizations, the percentages are lower for the Camarón, Cañada,

Chulul, and Esmeralda lakes, which measure <2 ha in size. The completeness results presented in Table 4 show 18 water bodies with a value over >80% with the HT filter and 18 with the Lee filter.

Overlap is another criterion (Table 5). The reference image is considered to be a template that at greater superposition will have a value close to 1. Superposition is defined as the total number of pixels that exist in both regions, divided by the sum of the areas of both regions. In the case of the VV and VH polarizations, the overlap values ranged from 0.7 to 0.96. However, with the VV polarization in descending mode, better results were obtained using the Hermite and Lee filters, with 10 and 9 lakes having an overlap value >0.9, respectively.

4.3 *Identification of Morphological Properties*

The shapes of the lagoons were studied based on the coastline parameter (SLD). Figure 8 shows this radar chart. SLD is useful because it is a morphological indicator that enables comparing changes that can occur in the shapes of water bodies over short time periods. All S1 methods are compared with the S2 reference in this radar chart (Table 5). In the case of the San Lorenzo Lagoon, the coastline value is >3, which may indicate that the shape of this water surface is mainly elliptical (uvalas landform). Many lagoons have values that are close to 1, which indicates that these are rounded lagoons and could be classified as small circular lagoons. In the literature, many of the lagoons in this study area are identified as having a doline landform, a very rounded shapes. Our previous field study found that many water bodies change their SLD due to connectivity or isolation processes related to seasonality. SAR can potentially be used to study these dynamic cycles.

5 Conclusions

This paper presented several methods for restoring S1 datasets. In particular, noise speckle reduction has an important effect on the restoration of SAR images. With the Hermite filter algorithm, the internal texture of water bodies is preserved as a homogenous area. The LWE maps that were obtained with the Hermite technique show that there were no problems with the pixels of the water/nonwater borders because the algorithm restored them, thereby achieving sharp edges and adequately separating the water/nonwater elements. With regard to the MSWB and SWB, these small regions are affected by noise. The Hermite filter enables restoring the homogenous internal values of the water body.

This study was able to evaluate and determine an optimal methodology for quantifying each LWE map. The reliability indices and the visual identification of reliability indicate that the LWE obtained with the new denoising approach provided better results with the HT, followed by the Lee filter, using descending orbit and VV polarization. With the given acquisition time of the descending orbit and the data acquisition geometry, all of the lakes in the study area could be adequately characterized.

Furthermore, this investigation contributes to the exploration of techniques for delineating MSWB and SWB located in high mountains and plains, such as the Montebello Lagoon system. Given the geographic characteristics and the abundant cloudiness in the study area, S1 SAR data are valuable for multitemporal monitoring in this region.

In the context of climate change, and considering the ecosystem services that are provided by MWB and SWB, it is important to conserve these ecosystems. The temporal analysis of this type of systems provides important information about how climate variability affects their ecological behavior.

6 Appendix

Comparison between the HT filter and Lee filter methods. Evaluation of the lagoons based on completeness (%), AA (%), overlap, and SLD.

Table 4 Evaluation of lagoons based on AA (%) and completeness measurements (%).

| Lagoon | Ascending orbit | | | | Descending orbit | | | | | | | |
| | AA (%) | | | | AA (%) | | | | Completeness (%) | | | |
	HERMITE-SIGMA0-DB-VH	HERMITE-SIGMA0-DB-VV	LEE-SIGMA0-DB-VH	LEE-SIGMA0-DB-VV	HERMITE-SIGMA0-DB-VH	HERMITE-SIGMA0-DB-VV	LEE-SIGMA0-DB-VH	LEE-SIGMA0-DB-VV	HERMITE-SIGMA0-DB-VH	HERMITE-SIGMA0-DB-VV	LEE-SIGMA0-DB-VH	LEE-SIGMA0-DB-VV
Lago Tziscao	96.17	97.72	96.5	99.65	98.65	99.51	98.78	99.32	95.58	95.65	95.78	96.54
San Lorenzo	82.15	62.77	81.82	45.79	90.3	92.48	90.05	92.38	88.83	90.19	88.83	90.34
Montebello	86.19	96.44	86.5	95.52	94.68	97.99	95.09	98.35	91.32	93.58	91.86	93.83
San José	87.27	72.79	86.73	62.47	92.19	91.19	91.16	90.57	91.83	90.82	90.95	90.44
Bosque Azul	82.28	94.43	82.12	90.77	88.9	94.53	88.8	94.13	86.76	90.82	86.89	90.62
Lago Pojol	84.35	98.24	84.78	99.35	88.18	92.45	88.72	94.29	83.69	86.17	84.4	87.64
Liquidambar	75.17	93	75.36	87.32	84.82	89.12	85.51	90.52	83.07	85.87	83.84	86.82
Poza Azul	77.51	95.04	77.97	99.98	85.59	89.9	85.46	91.4	79.46	81.23	80.58	82.19
Chanujabab	89.61	80.76	90.39	72.47	92.96	97.1	92.16	97.24	89.62	91.99	89.01	92.69
Balantetic	65.86	96.45	61.23	98.48	65.48	67.45	67.08	70.44	65.47	67.19	67.07	70.22
Kikchayil	72.23	98.15	72.08	96.1	94.29	95.31	93.37	95.31	86.86	90.74	86.44	91.61
Chaj Chaj	80.59	98.85	79.97	89.08	80.54	88.05	79.65	88.05	79.52	86.06	79.2	86.35
La Encantada	67.52	94.18	64.8	86.92	93.45	97.62	94.31	97.85	85.97	90.64	86.85	90.35
El Perol	72.62	93.88	69.16	85.74	89.99	94.06	92.76	90.54	73.35	82.43	71.29	83.88
Agua Amarilla	72.44	96.58	70.01	96.05	72.17	84.68	69.14	83.41	70.34	80	67.96	78.46

Table 4 (*Continued*).

| | Ascending orbit | | | | Descending orbit | | | | | | | |
| | AA (%) | | | | AA (%) | | | | Completeness (%) | | | |
Lagoon	HERMITE-SIGMA0-DB-VH	HERMITE-SIGMA0-DB-VV	LEE-SIGMA0-DB-VH	LEE-SIGMA0-DB-VV	HERMITE-SIGMA0-DB-VH	HERMITE-SIGMA0-DB-VV	LEE-SIGMA0-DB-VH	LEE-SIGMA0-DB-VV	HERMITE-SIGMA0-DB-VH	HERMITE-SIGMA0-DB-VV	LEE-SIGMA0-DB-VH	LEE-SIGMA0-DB-VV
Internacional	69.75	75	68.99	94.05	92.05	89.55	86.15	88.89	81.5	83.03	79.04	84.29
Agua Tinta	71.26	87.92	70.95	97.05	94.68	97.99	76.81	91.23	74.19	79.81	72.78	80.79
Ensueño	57.42	86.24	45.71	74.95	85.67	90.3	84.58	90.55	77.65	89.83	78.45	91.14
Yuchan	46.62	98.87	31.49	86.08	87.52	96.93	84.43	97.42	77.9	85.55	75.29	81.82
Camarón	<40	<40	<40	<40	96.27	80.00	99.11	83.28	84.78	89.59	84.24	87.13
La Cañada	<40	<40	<40	<40	75.34	88.89	72.73	89.46	64.48	74.49	64.57	76.15
Chulul	42.49	98.8	39.33	87.55	71.35	80.74	63.65	83.79	52.11	61.63	48.05	64.1
La Esmeralda	<40	<40	<40	<40	72.95	82.62	64.26	79.08	69.83	64.65	63.45	63.34
Number of lagoons >80%	8	17	7	16	18	22	16	21	12	18	12	18

Table 5 Evaluation of lagoons based on overlap measurements and shoreline development.

Lagoon	Descending orbit								
	Overlap				SLD				
	HERMITE-SIGMA0-DB-VH	HERMITE-SIGMA0-DB-VV	LEE-SIGMA0-DB-VH	LEE-SIGMA0-DB-VV	Reference	HERMITE-SIGMA0-DB-VH	HERMITE-SIGMA0-DB-VV	LEE-SIGMA0-DB-VH	LEE-SIGMA0-DB-VV
Lago Tziscao	0.96	0.96	0.85	0.89	2.25	2.49	2.7	2.29	2.23
San Lorenzo	0.93	0.94	0.93	0.94	3.82	3.92	3.96	3.77	3.79
Montebello	0.94	0.95	0.94	0.94	2.27	2.53	2.36	2.33	2.31
San José	0.96	0.95	0.95	0.93	1.62	1.76	1.76	1.76	1.8
Bosque Azul	0.92	0.93	0.92	0.93	2.13	2.38	2.32	2.28	2.28
Lago Pojol	0.89	0.9	0.89	0.9	1.86	2.14	2.16	1.95	2.15
Liquidambar	0.9	0.91	0.9	0.91	2.54	2.9	2.86	2.91	2.85
Poza Azul	0.86	0.86	0.87	0.86	1.82	2.22	2.28	2.01	2.14
Chanujabab	0.93	0.93	0.93	0.94	1.55	1.51	1.66	1.45	1.52
Balantetic	0.79	0.8	0.8	0.82	1.62	1.86	1.89	1.93	2
Kikchayil	0.89	0.89	0.89	0.9	1.89	2	2.01	2	1.94
Chaj Chaj	0.88	0.92	0.88	0.91	1.55	1.56	1.5	1.45	1.44
La Encantada	0.89	0.9	0.89	0.89	1.2	1.32	1.24	1.27	1.3
El Perol	0.77	0.8	0.74	0.8	1.13	1.49	1.31	1.29	1.25
Agua Amarilla	0.82	0.87	0.8	0.86	1.1	1.22	1.07	1.16	1.25

Table 5 (*Continued*).

Lagoon	Descending orbit								
	Overlap				SLD	SLD		SLD	
	HERMITE-SIGMA0-DB-VH	HERMITE-SIGMA0-DB-VV	LEE-SIGMA0-DB-VH	LEE-SIGMA0-DB-VV	Reference	HERMITE-SIGMA0-DB-VH	HERMITE-SIGMA0-DB-VV	LEE-SIGMA0-DB-VH	LEE-SIGMA0-DB-VV
Internacional	0.85	0.88	0.85	0.89	1.03	1.41	1.32	1.35	1.25
Agua Tinta	0.82	0.84	0.82	0.84	1.03	1.19	1.1	1.18	1.08
Ensueño	0.84	0.86	0.85	0.87	1.04	1.35	1.19	1.21	1.25
Yuchan	0.83	0.84	0.82	0.83	1.24	1.3	1.24	1.47	1.3
Camarón	0.83	0.81	0.84	0.8	1.1	1.12	1.11	1.08	1.11
La Cañada	0.74	0.79	0.75	0.8	1.03	1.26	1.13	1.25	1.28
Chulul	0.61	0.68	0.59	0.7	1.02	1.21	1.16	1.16	1.24
La Esmeralda	0.81	0.71	0.77	0.7	1.04	1.12	1.28	1.13	1.49
Number of lagoons >0.90	7	10	6	9	—	—	—	—	—

Acknowledgments

References

1. J. Biggs, S. Von Fumetti, and M. Kelly-Quinn, "The importance of small waterbodies for biodiversity and ecosystem services: implications for policy makers," *Hydrobiologia* **793**, 3–39 (2017).
2. M. Kelly-Quinn, J. Biggs, and S. Fumetti, "The importance of small water bodies," *Hydrobiologia* **793**(1), 1–2 (2017).
3. J.-F. Pekel et al., "High-resolution mapping of global surface water and its long-term changes," *Nature* **540**, 418–422 (2016).
4. F. Bioresita et al., "A method for automatic and rapid mapping of water surfaces from Sentinel-1 imagery," *Remote Sens.* **10**, 217 (2018).
5. K. Uddin, M.-A. Matin, and F. J. Meyer, "Operational flood mapping using multi-temporal Sentinel-1 SAR images: a case study from Bangladesh," *Remote Sens.* **11**, 1581 (2019).
6. A. Dasgupta et al., "Towards operational SAR-based flood mapping using neuro-fuzzy texture-based approaches," *Remote Sens. Environ.* **215**, 313–329 (2018).
7. S. Solbø and I. Solheim, "Towards operational flood mapping with satellite SAR," in *Proc. Envisat & ERS Symp.*, Salzburg, Austria, ESA SP-572 (2005).
8. A. Ogilvie et al., "Surface water monitoring in small water bodies: potential and limits of multi-sensor Landsat time series," *Hydrol. Earth Syst. Sci.* **22**, 4349–4380 (2018).
9. E. M. Pôssa and P. Maillard, "Precise delineation of small water bodies from Sentinel-1 data using support vector machine classification," *Can. J. Remote Sens.* **44**(3), 179–190 (2018).
10. J. S. Lee, "Speckle analysis and smoothing of synthetic aperture radar images," *Comput. Graphics Image Process.* **17**(1), 24–32 (1981).
11. B. Escalante-Ramírez and A. A. López-Caloca, "The Hermite transform: an efficient tool for noise reduction and image fusion in remote sensing," in *Image Processing for Remote Sensing*, C. H. Chen, Ed., pp. 537–555, CRC Press, Boca Raton, Florida (2007).
12. S. Yeong-Sun, S. Hong-Gyoo, and P. Choung-Hwan, "Efficient water area classification using Radarsat-1 SAR imagery in a high relief mountainous environment," *Photogramm. Eng. Remote Sens.* **73**(3), 285–296 (2007).
13. L. Wentao, Y. Qiuze, and Y. Wenxian, "Water extraction in SAR images using GLCM and support vector machine," in *IEEE 10th Int. Conf. Signal Process. Proc.*, pp. 740–743 (2010).
14. L. Mora, R. Bonifaz, and R. López-Martínez, "Unidades geomorfológicas de la cuenca del Río Grande de Comitán, Lagos de Montebello, Chiapas-México," *Bol. Soc. Geol. Mex.* **68**(3), 377–394 (2016).
15. J. Alcocer et al., "Bathymetric and morphometric surveys of the Montebello Lakes, Chiapas," *J. Limnol.* **75**(1s), 56–65 (2016).
16. L. D. Calderón et al., "Cartografía geomorfológica a escala 1:50000 del Parque Nacional Lagunas de Montebello, Chiapas (México)," *Bol. Soc. Geol. Mex.* **66**(2), 263–277 (2014).
17. https://earthdata.nasa.gov/eosdis/daacs/asf.
18. https://scihub.copernicus.eu/dhus/#/home.
19. A. Robak et al., "The detection of water on Sentinel-2 imagery based on water indices," *Teledetekcja Środowiska* **55**, 59–72 (2016).
20. D. T. Kuan et al., "Adaptive noise smoothing filter for images with signal-dependent noise," in *IEEE Trans. Pattern Anal. Mach. Intell.* **PAMI-7**(2), 165–177 (1985).
21. A. Lopes, R. Touzi, and E. Nezry, "Adaptive speckle filters and scene heterogeneity," in *IEEE Trans. Geosci. Remote Sens.* **28**(6), 992–1000 (1990).

22. P. Camarillo-Sandoval, A. Varela-López, and B. Escalante-Ramírez, "Adaptive multiplicative-noise reduction in SAR images with polynomial transforms," in *IGARSS'98, IEEE Geosci. and Remote Sens. Soc., Proc. (Cat. No.98CH36174)*, pp. 1171–1173 (1998).

23. J. A. Franco et al., "SAR images filtering and segmentation: a multiresolution and contextual approach," in *Proc. IEEE Int. Geosci. and Remote Sens. Proc. (Cat. No.01CH37217)*, pp. 2304–2306 (2001).

24. J. L. Silván-Cárdenas and B. Escalante-Ramírez, "The multiscale Hermite transform for local orientation analysis," *IEEE Trans. Image Process.* **15**(5), 1236–1253 (2006).

25. A. Castro-Valdez and J. Álvarez-Borrego, "Identification of phytoplankton species using Hermite transform," *Ukr. J. Phys. Opt.* **19**(2), 106–120 (2018).

26. H. Feng, B. Hou, and M. Gong, "SAR image despleckling based on local homogeneous-region segmentation by using pixel-relativity measurement," *IEEE Trans. Geosci. Remote Sens.* **49**(7), 2724–2737 (2011).

27. F. Fillipponi, "Sentinel-1 GRD preprocessing workflow," *Proceedings* **18**, 11 (2019).

28. A. Wendleder et al., "TanDEM-X water indication mask: generation and first evaluation results," *IEEE J. Sel. Top. Appl. Earth Obs. Remote Sens.* **6**(1), 171–179 (2013).

29. D. M. McKeown and J. L. Denlinger, "Map-guided feature extraction from aerial imagery," in *Proc. Second IEEE Comput. Soc. Workshop Comput. Vision: Represent. and Control*, Also available as Technical Report CMU-CS-84-11 (1984).

30. H. Cao et al., "Operational flood detection using Sentinel-1 SAR data over large areas," *Water* **11**(4), 786 (2019).

Alejandra A. López-Caloca received her PhD from the UNAM in 2007, in the field of electrical engineering, in the digital treatment of images and signals discipline. Currently, she works as a researcher and postgraduate teacher at Centro de Investigación en Ciencias de Información Geoespacial. She is also working in basic and applied research lines related to spatial analysis, data fusion, images fusion, dynamic systems, spatiotemporal analysis, change detection, digital classifiers including optics, SAR, and InSAR.

Boris Escalante-Ramírez received his PhD from the Technical University of Eindhoven in 1992. He is currently a full professor in the Signal Processing Department of the School of Engineering, Universidad Nacional Autónoma de México. His research areas include computational models for image processing and computer vision.

Pilar Henao received her BS degree in geography from the Universidad del Valle, Colombia, in 2012 and her postgraduate degree in geomatics from CentroGeo, Mexico, in 2017. She is currently pursuing her MS thesis at the same research center. Her scientific interests include the triggers in several phenomena and their response to a specific approach, which allows the adjustment of variables for the proposal of efficient monitoring methodologies for informed decision-making.